JCI insight

RESEARCH ARTICLE

TAZ is required for lung alveolar epithelial cell differentiation after injury

Tianhe Sun,[1] Zhiyu Huang,[2] Hua Zhang,[2] Clara Posner,[1] Guiquan Jia,[3] Thirumalai R. Ramalingam,[3] Min Xu,[2] Hans Brightbill,[2] Jackson G. Egen,[1] Anwesha Dey,[4] and Joseph R. Arron[1]

[1]Department of Immunology, [2]Department of Translational Immunology, [3]Department of Biomarker Discovery OMNI, and [4]Department of Oncology, Genentech, 1 DNA Way, South San Francisco, California, USA.

The lung is a relatively quiescent organ during homeostasis but has a remarkable capacity for repair after injury. Alveolar epithelial type I cells (AEC1s) line airspaces and mediate gas exchange. After injury, they are regenerated by differentiation from their progenitors — alveolar epithelial type II cells (AEC2s) — which also secrete surfactant to maintain surface tension and alveolar patency. While recent studies showed that the maintenance of AEC2 stemness is Wnt dependent, the molecular mechanisms underlying AEC2-AEC1 differentiation in adult lung repair are still incompletely understood. Here, we show that WWTR1 (TAZ) plays a crucial role in AEC differentiation. Using an in vitro organoid culture system, we found that tankyrase inhibition can efficiently block AEC2-AEC1 differentiation, and this effect was due to the inhibition of TAZ. In a bleomycin-induced lung injury model, conditional deletion of TAZ in AEC2s dramatically reduced AEC1 regeneration during recovery, leading to exacerbated alveolar lesions and fibrosis. In patients with idiopathic pulmonary fibrosis (IPF), decreased blood levels of the receptor for advanced glycation end products (RAGE), a biomarker of AEC1 health, were associated with more rapid disease progression. Our findings implicate TAZ as a critical factor involved in AEC2-to-AEC1 differentiation, and hence the maintenance of alveolar integrity after injury.

Introduction

Idiopathic pulmonary fibrosis (IPF) is a progressive disease with a complex and incompletely understood etiology. A conceptual model for IPF pathogenesis implicates defective alveolar epithelial cell (AEC) repair after repetitive injuries, resulting in compromised gas exchange, loss of barrier function, inflammation, extracellular matrix (ECM) accumulation, and progressive interstitial fibrosis. There is evidence for "reactivation" of multiple pathways involved in embryonic lung development in IPF, e.g., Hh, Notch, Wnt, and Hippo. Genetic studies strongly implicate alveolar epithelial type II cell–associated (AEC2-associated) genes in familial and sporadic forms of pulmonary fibrosis (1), suggesting that compromised epithelial regenerative capacity is a key event driving IPF pathogenesis.

The alveolar epithelium is maintained and repaired by proliferation and hyperplasia of AEC2s, followed by differentiation into alveolar epithelial type I cells (AEC1s). In epithelial injury models, multiple progenitor cell populations have been proposed to differentiate into AEC2s (2–5). AEC1s, on the other hand, were demonstrated to differentiate from AEC2s four decades ago (6, 7), further supported by recent observations using in vivo lineage-tracing technology (8, 9). However, the molecular mechanisms underlying AEC2-AEC1 differentiation are poorly understood. Recently, Hogan and colleagues described a 3D alveolosphere organoid culture system, in which lineage-labeled mouse AEC2s were seeded with mouse PDGFRα$^+$ lung fibroblasts in Matrigel. 3D spheroids develop within 14 days, with SPC$^+$ (surfactant protein C) AEC2s on the outside and AEC1s expressing characteristic markers, including HOPX, AQP5, and PDPN, inside the lumen (Figure 1A and ref. 8). We employed this system to screen small-molecule inhibitors of various signaling pathways to identify potentially novel factors involved in AEC biology, including AEC2 proliferation and differentiation.

Results

To facilitate screening, we substituted normal human lung fibroblasts (NHLFs) for mouse primary PDGFRα$^+$ lung fibroblasts as the stromal cells in the culture. Alveolospheres exhibited comparable growth and differentiation phenotypes to those reported by Barkauskas et al. (ref. 8 and Figure 1, B–D and H).

Authorship note: ZH and HZ contributed equally to this work.

Conflict of interest: TS, ZH, HZ, GJ, TRR, MX, HB, AD, and JRA are current employees of Genentech and shareholders in Roche. JGE is a current employee of Amgen Inc (SCIENCE EDITOR: Please confirm the COI statement.).

Submitted: March 11, 2019
Accepted: June 13, 2019
Published: July 25, 2019.

Reference information: *JCI Insight*. 2019;4(14):e128674. https://doi.org/10.1172/jci.insight.128674.

In this mixed-species coculture, gene expression profiles of AECs could be distinguished from those in the stromal cells using species specific qPCR probes.

Among compounds screened, IWR-1, a selective tankyrase inhibitor (10), significantly inhibited AEC2-AEC1 differentiation when added continuously to the cultures. In the control cultures, AEC1s differentiated from the exterior AEC2s and localized toward the inner lumen of the spheroids. Possibly due to the long and squamous shape of AEC1s and their interaction with AEC2s, the surface of those spheroids became spiny and irregular (Figure 1, C, D, and H). However, in IWR-1–treated cultures, we observed rounded spheres with smooth surfaces (Figure 1, E–G). Using confocal microscopy, we found that in the IWR-1–treated organoids, HOPX$^+$ AEC1s were absent inside the lumen, while peripheral SPC$^+$ AEC2s were intact (Figure 1, I vs. H, and Supplemental Videos 1 and 2; supplemental material available online with this article; https://doi.org/10.1172/jci.insight.128674DS1). The ratios of AEC2-specific (*Spc*) to AEC1-specific (e.g., *Hopx*, *Aqp5*, and *Pdpn*) gene expression were significantly increased in IWR-1–treated alveolospheres (Figure 1J). This effect was due to failure of AEC2-AEC1 differentiation and not to a toxic effect of IWR-1 on AEC2s, as the proliferation rates of AEC2s were comparable with and without IWR-1 treatment (Supplemental Figure 1A). When IWR-1 was applied after AEC1 differentiation, AEC1s remained intact in the spheroids, suggesting that IWR-1 was not selectively toxic to AEC1s (Supplemental Figure 1B). Prior studies have shown that isolated AEC2s acquire AEC1 morphological features and expression markers after growing on regular tissue culture plates (11, 12). We observed many squamous AQP5$^+$ AEC1-like cells after culturing AEC2s for 5 days, but IWR-1 treatment resulted in rounded undifferentiated cells with very weak AQP5 expression (Figure 1K and ref. 13). Furthermore, we did not observe significant effects of IWR-1 on cell number (Supplemental Figure 1C). While this culture condition typically promotes AEC1 differentiation, IWR-1–treated cells retained AEC2 marker expression (SPC$^+$) after 5 days of culture (Supplemental Figure 1D). Taken together, these data show that IWR-1 blocks AEC2-AEC1 differentiation in vitro.

To account for potential off-target effects, we tested other available tankyrase inhibitors (XAV939, JW55) and observed similar phenotypes to cultures treated with IWR-1. In contrast, we did not observe similar effects in cultures treated with PJ34 (a broad-spectrum PARP inhibitor with >100× selectivity for PARP1 over tankyrase; ref. 14), PNU-74654 (β-catenin/TCF inhibitor), or IWR-1-exo (nonfunctional diastereomer of IWR-1; Figure 2, A and B).

Tankyrase plays a regulatory role in both the Wnt/β-catenin and Hippo/YAP/TAZ signaling pathways (10, 15). Specifically, it attaches poly(ADP-ribose) groups (PARsylates) Axin, a limiting component of the β-catenin destruction complex and targets it for degradation. Therefore, tankyrase inhibitors can stabilize the destruction complex and promote β-catenin degradation. Furthermore, the same destruction complex can also serve as a cytoplasmic sink for YAP/TAZ and promote TAZ degradation (15, 16).

To assess whether IWR-1 inhibition of AEC2-AEC1 differentiation in vitro was attributable to canonical Wnt pathway inhibition, we seeded the organoid culture with LysoTracker-sorted AEC2s from *Ctnnb1*$^{fl/fl}$ mice. LysoTracker has been used previously to isolate AEC2s from nonlineage-labeled mice for organoid culture (17), and we observed that over 95% of lineage-labeled AEC2s were also LysoTracker$^+$ (Supplemental Figure 2). We introduced CRE recombinase via adenovirus at the onset of culture to delete the floxed alleles (ref. 18 and Supplemental Figure 3, A and B). Most spheroids exhibited clonal gene deletion, suggesting that adenoviral infection and Cre-driven recombination occurs at an early single AEC2 stage (Supplemental Figure 3, A and B, and Figure 2C). More than half of spheroids had deleted β-catenin in culture (Supplemental Figure 3C), but we observed AEC1 differentiation in the both β-catenin$^{+/+}$ and β-catenin$^{-/-}$ spheroids based on individual spheroid confocal images (Figure 2C and Supplemental Videos 3 (β-catenin$^{+/+}$) and 4 [β-catenin$^{-/-}$])and full-plate images (Figure 2D). We did not observe significant differences in AEC2:AEC1 ratios between WT and β-catenin$^{-/-}$ spheroids by cell-type specific gene expression (Figure 2E). Consistent with a recent report showing that lack of Wnt signaling may actually promote AEC2-AEC1 differentiation under steady-state conditions (19), we conclude that β-catenin inhibition was not responsible for the defective AEC2-AEC1 differentiation phenotype observed with tankyrase inhibitors.

As the β-catenin destruction complex can also regulate YAP/TAZ in a tankyrase-dependent manner (15, 16), we immunostained spheroids to assess whether YAP or TAZ might be involved in AEC2-AEC1 differentiation. While YAP was not detected in the AECs (Figure 3A), TAZ localized to the nuclei of AEC1s inside the lumen of the spheroids but not in AEC2s on the surface (Figure 3B), suggesting that TAZ may play a role during differentiation. We could not detect TAZ in spheroids treated with IWR-1 (Figure 3C). To assess the specific role of TAZ in AEC2-AEC1 differentiation, we generated conditional

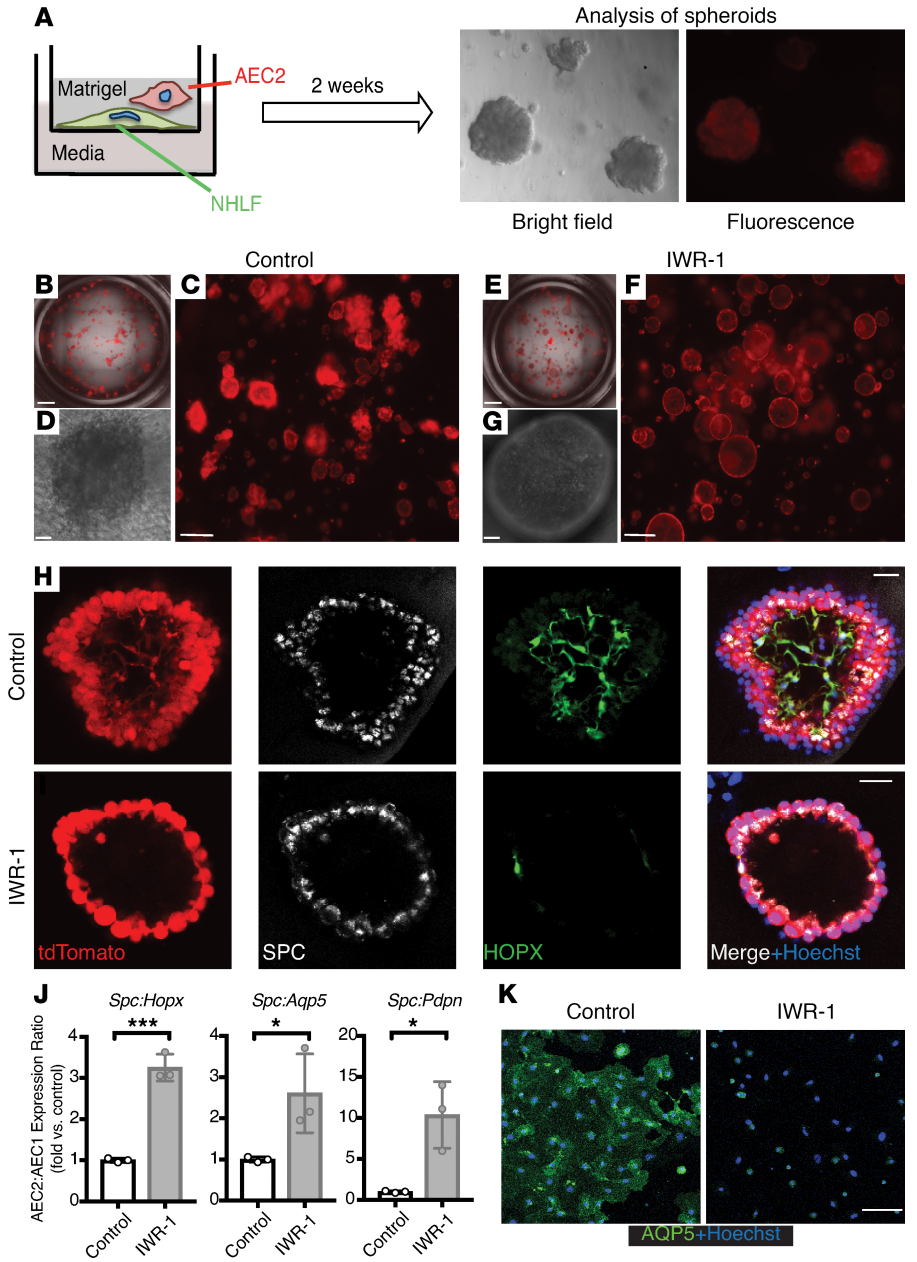

Figure 1. IWR-1 inhibits AEC2-to-AEC1 differentiation in vitro. TdTomato$^+$ lineage-labeled AEC2s were sorted from SPC-CreERT2; Rosa-lsl-tdTomato mouse lungs after tamoxifen administration. (**A**) 3D alveolar spheroid culture schematic: AEC2s were cultured in Matrigel with NHLF for 2 weeks or until alveolospheres developed. (**B**–**G**) Cells were treated with either control (DMSO) (**B**–**D**) or IWR-1 (**E**–**G**) throughout culture. Merged bright-field (BF) and fluorescence (FL) full-plate images (**B** and **E**) and FL close-ups (**C** and **F**) show the overall difference in shapes of the cultured spheroids under these 2 conditions. (**D** and **G**) Representative high-power BF images emphasize the distinct smooth surface of spheroids cultured with IWR-1 as compared to controls. (**H** and **I**) Whole spheroids were immunostained for AEC2 (SPC), AEC1 (HOPX), and Nuclei (Hoechst). Single focal planes of *Z*-stack images are shown. Full *Z*-stack images are available as Supplemental Videos 1 (control) and 2 (IWR-1). (**J**) Gene expression ratios (mean ± SD, 3 biological replicates) between *Spc* and *Hopx*, *Aqp5*, and *Pdpn* were used to quantify the AEC2 versus AEC1 composition of each well. No signals were detected with NHLF alone with these mouse qPCR probes. $^*P < 0.05$; $^{***}P < 0.001$ (unpaired 2-tailed Student's *t* tests). (**K**) Sorted AEC2s from C57B6 mice were cultured directly on cell culture–treated slides without (control) or with IWR-1 for 5 days in the presence of 10% serum. Cells were immunostained for AQP5 and nuclei were counterstained with Hoechst. Scale bars: 1 mm (**B** and **E**); 300 μm (**C** and **F**); 30 μm (**D** and **G**–**I**); 100 μm (**K**).

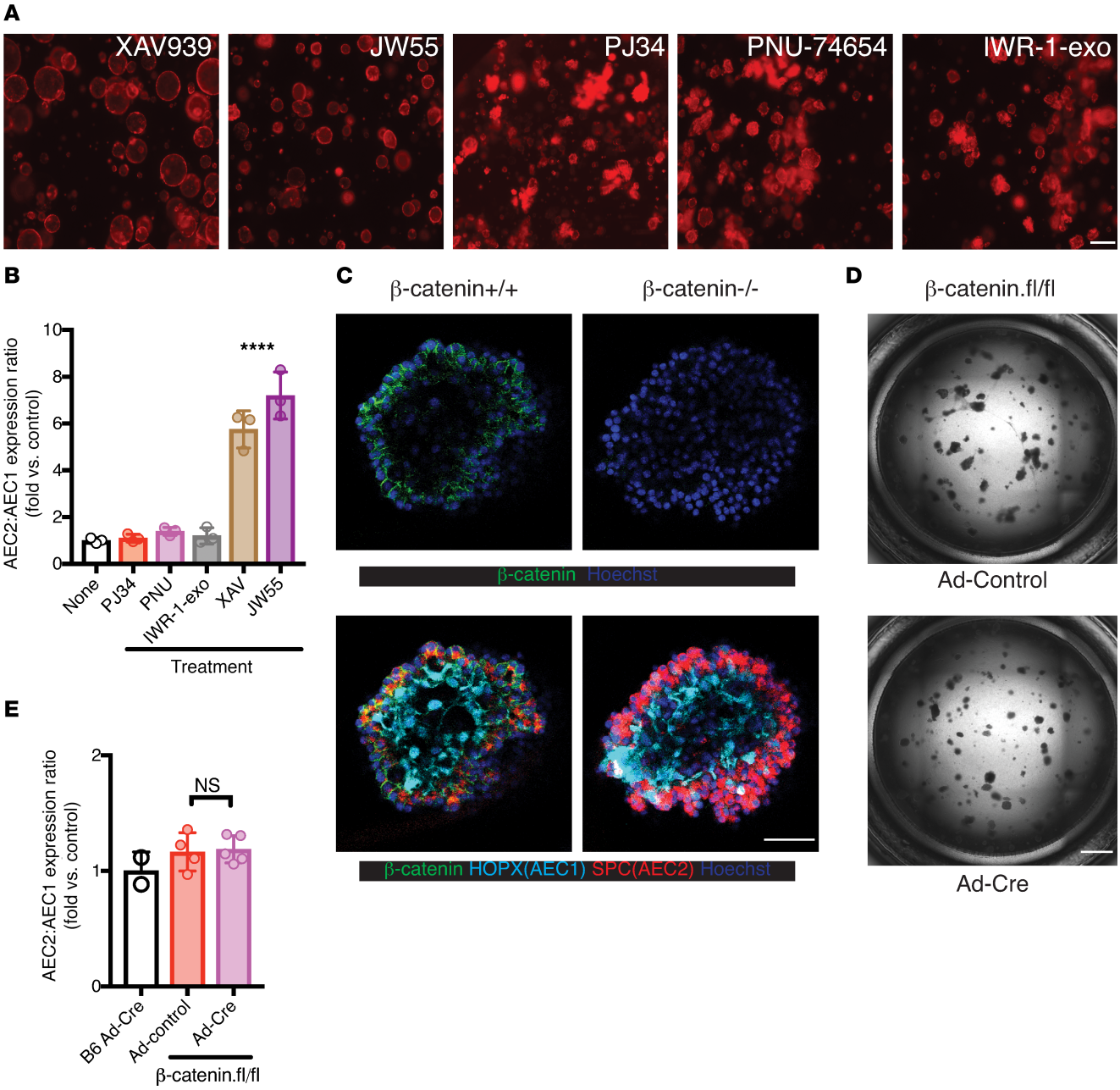

Figure 2. Blockade of AEC2-to-AEC1 differentiation by tankyrase inhibition is not due to β-catenin inhibition. (**A** and **B**) Cells were treated as in Figure 1, with additional small-molecule inhibitors as indicated. FL images (**A**) at the end of cultures are shown. (**B**) Quantification of different culture conditions by AEC2 versus AEC1 gene expression ratios as in Figure 1J (*Spc*/*Pdpn*; mean ± SD, 3 biological replicates). ****$P < 0.001$ for both XAV and JW55 conditions versus none (1-way ANOVA with Tukey's test). (**C**–**E**) β-Catenin$^{fl/fl}$ AEC2s were infected with control adenovirus (Ad-control) or Ad-Cre in the spheroid culture. (**C**) Confocal images show normal AEC1 differentiation in a β-catenin$^{-/-}$ spheroid. Note the β-catenin membrane-proximal expression in β-catenin$^{+/+}$ but not in β-catenin$^{-/-}$ spheroids. Full *Z*-stack images are available as the Supplemental Videos 3 (β-catenin$^{+/+}$) and 4 (β-catenin$^{-/-}$). (**D**) BF full-plate images show similar overall spheroid shapes after treatments. (**E**) Quantification of AEC2 versus AEC1 gene expression ratios show no differences between treatments (*Spc*/*Pdpn*; mean ± SD, 4–o 5 biological replicates) NS (unpaired 2-tailed Student's *t* tests). Scale bars: 300 μm (**A**); 50 μm (**C**); 1 mm (**D**).

TAZ-KO mice by crossing *Taz*$^{fl/fl}$ to *SPC-CreERT2*; *Rosa26tdTomato* mice (SPC-Taz.KO-Tm mice). TAZ was efficiently deleted from the tdTomato$^+$ AEC2s after tamoxifen induction (Supplemental Figure 4). In organoid cultures seeded with TAZ$^{-/-}$ tdTomato$^+$ AEC2s, we observed similar spheroid phenotypes as with tankyrase inhibition in WT AECs, i.e., rounded spheres with a high AEC2-to-AEC1 gene expression ratio, and no AEC1s inside the spheroids (Figure 4, A–C). This strongly suggests that TAZ is required for AEC2-to-AEC1 differentiation and that TAZ inhibition may explain the effect of tankyrase inhibitors. When we cultured sorted AEC2s on culture plates, TAZ was activated (nuclear localized) on day 5 (Figure 4D) when

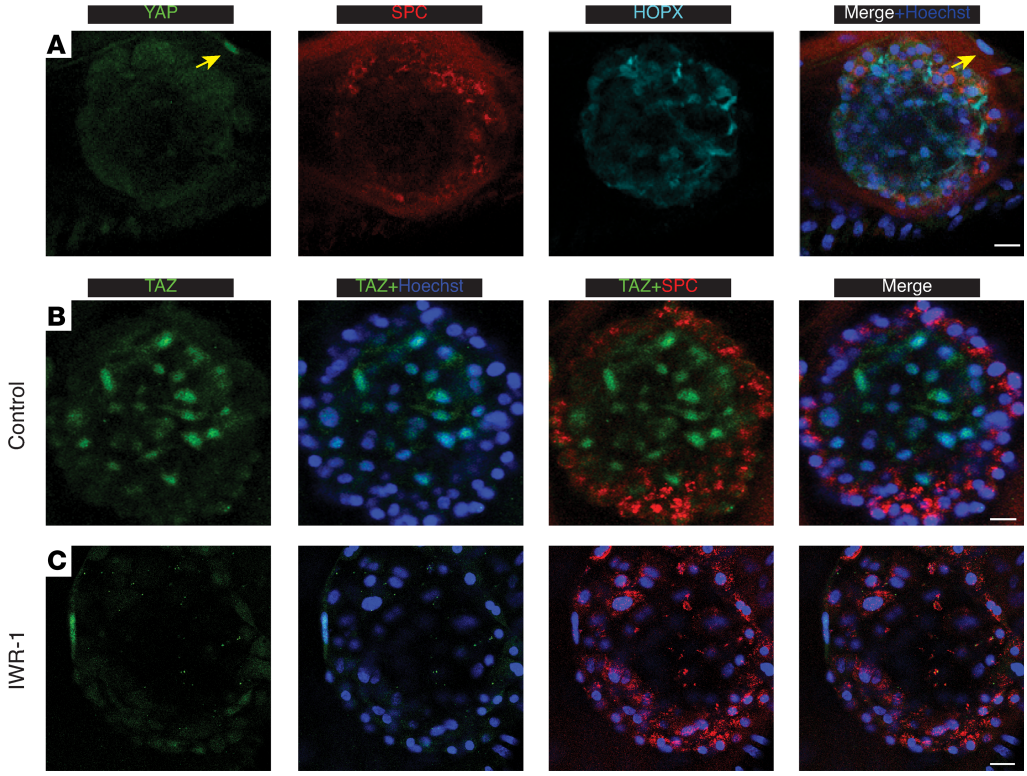

Figure 3. TAZ, but not YAP, is expressed (nuclear localized) during differentiation in AEC organoid culture. (**A**) Untreated C57B6 alveolospheres were immunostained for YAP, SPC, HOPX, and Hoechst (nuclei). Note: Sporadic stromal NHLF cells expressed YAP in their nuclei as indicated by the yellow arrow. (**B** and **C**) C57B6 alveolospheres were immunostained for TAZ, SPC, and Hoechst. Cultures were treated with control (DMSO) (**B**) or IWR-1 (**C**), respectively. Scale bars: 20 μm.

squamous AQP5$^+$ AEC1-like cells developed (Figure 4E). TAZ$^{-/-}$ AEC2 cultures contained fewer AEC1-like cells and more small undifferentiated cuboidal cells with weak *AQP5* expression (Figure 4, E and F), but there were similar overall cell numbers as in WT cultures, suggesting that TAZ deficiency did not affect survival (Figure 4G). Taken together, these data suggest that the effect of tankyrase inhibition on AEC2-AEC1 differentiation is dependent on TAZ and not β-catenin.

Intratracheal (i.t.) bleomycin installation is a commonly used murine model of lung injury, repair, and fibrosis. Bleomycin initially damages the alveolar epithelium, followed by inflammation and interstitial fibrosis. To assess the role of TAZ in AEC2s during lung epithelial repair, as well as its subsequent effects on fibrosis, we delivered i.t. bleomycin to SPC-Taz.KO-Tm and control mice with a WT *Taz* locus (SPC-WT-Tm mice). In the untreated group, TAZ was detected in very few tdTomato-labeled AEC2s (0.5% ± 0.24%, mean ± SEM, Figure 5, A and C). In contrast, TAZ was expressed in the majority of tdTomato$^+$ cells 10 days after bleomycin injury (54% ± 2.6%, mean ± SEM, Figure 5, B and C). At that time point, the lineage-traced cells were SPC$^+$ and RAGE$^-$, indicating they were still AEC2s (Supplemental Figure 5). These TAZ$^+$ AEC2s were more abundant in actively regenerating regions, where increased numbers of tdTomato$^+$ alveoli were observed. Many TAZ$^+$ AEC2s were found adjacent to tdTomato$^+$ newly regenerated AEC1s, suggesting that they may be in an actively differentiating state (Figure 5B and Supplemental Figure 5). While most TAZ$^+$ cells were tdTomato$^+$ and exhibited nuclear localization of TAZ, we did observe sporadic cytoplasmically localized TAZ in tdTomato$^+$ AEC2 (Figure 5B, inset). YAP, on the other hand, was not detected in AECs after bleomycin injury (Figure 5D). Taken together, these observations suggest that TAZ is activated in AEC2s upon epithelial injury and TAZ$^+$ AEC1s developing in alveolosphere lumens in vitro may reflect AECs in the process of differentiation in vivo. Under homeostatic conditions, the non-AEC2-traced (tdTomato$^-$) TAZ$^+$ cells in the control group are mainly located in interstitial areas adjacent to alveoli (Figure 5A, inset), suggesting that TAZ may play a distinct role in stromal cells. Next, we quantified newly regenerated or repaired alveoli in both strains after bleomycin injury. In comparison with WT mice, alveoli marked by tdTomato$^+$ AEC1s were dramatically reduced in SPC-Taz.KO-Tm mice (20.2% ± 1.7% vs. 6.9% ± 0.75%; mean ± SEM, Figure 5, E–G). In particular, there

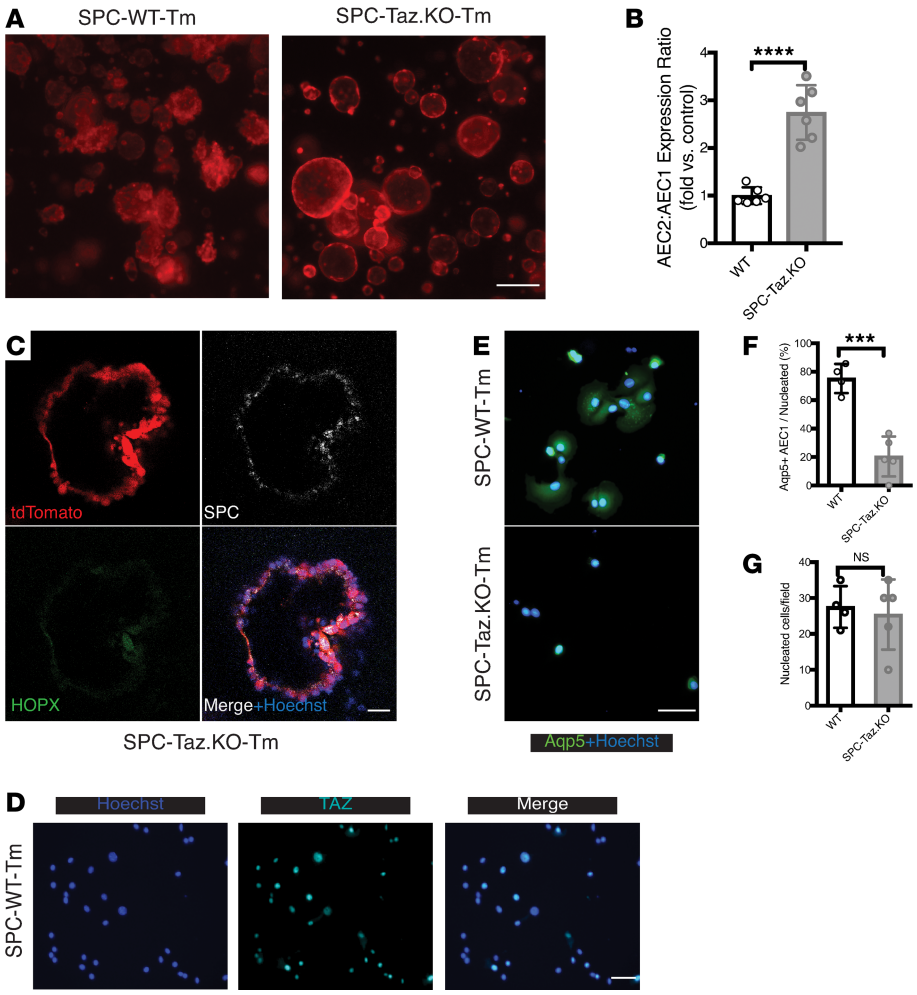

Figure 4. TAZ is required for AEC2-to-AEC1 differentiation in vitro. (**A**–**C**) AEC2s sorted from SPC-WT-Tm or SPC-Taz.KO-Tm mice. (**A**) FL images of the spheroids from the 3D culture are shown. (**B**) Quantification of AEC2:AEC1 gene expression ratios (*Spc/Pdpn;* mean ± SD, 6 biological replicates). (**C**) Confocal images show lack of HOPX$^+$ AEC1s in the lumen in the SPC-Taz.KO-Tm sphere. (**D**–**G**) Sorted AEC2s from SPC-WT-Tm or SPC-Taz.KO-Tm mouse lungs directly plated on glass for 5 days. Cells were immunostained for TAZ (**D**) or AQP5 (**E**) after 5 days culture on plate. (**F**) Percent (mean ± SD) of AEC1s (large, squamous, AQP5$^+$) were quantified (n = 4 mice [WT]; n = 5 mice [SPC-Taz.KO]). (**G**) Quantification of numbers of nucleated cells per field from the two mouse strains. ****$P < 0.0001$; ***$P < 0.001$; NS (unpaired 2-tailed Student's t tests). Scale bars: 300 μm (**A**); 30 μm (**C**); 50 μm (**D** and **E**).

were substantially fewer fields exhibiting abundant regenerated or repaired alveoli in SPC-Taz.KO-Tm mice, suggesting a defective repair process in areas with greater damage (Figure 5, F and G). Morphologically, the newly regenerated AEC1s in the SPC-Taz.KO mice were often shorter and lacked full extension, although it is unclear whether they were functionally compromised (Figure 5, E and F, inset). On the other hand, AEC2 proliferation in those mice was comparable to WT (Ki67$^+$ AEC2s: 6.1% ± 0.49% vs. 6.2% ± 1.04%, mean ± SEM, Supplemental Figure 6, A and B). Taken together, these results suggest that TAZ deficiency inhibits AEC2-to-AEC1 differentiation in vivo during alveolar repair after bleomycin injury.

To assess whether defective epithelial repair can contribute to fibrogenesis, we examined lungs 22 days after bleomycin injury, when ECM accumulation peaks. To visualize the relationship between alveolar structural alteration and fibrotic lesions, we immunostained lung sections for alveoli (RAGE to mark AEC1s) and collagen deposition (collagen I). Compared with WT controls treated with bleomycin, areas of alveolar destruction were more widespread in SPC-Taz.KO mice, revealed by the loss of RAGE staining (Figure 6A, enlarged, yellow outlines). Regions of decreased RAGE staining exhibited substantially greater collagen deposition in SPC-Taz.KO mice, resulting in more extensive fibrotic lesions than in WT mice (Figure 6A and Supplemental Figure 7). To quantify active fibrogenesis, we administered

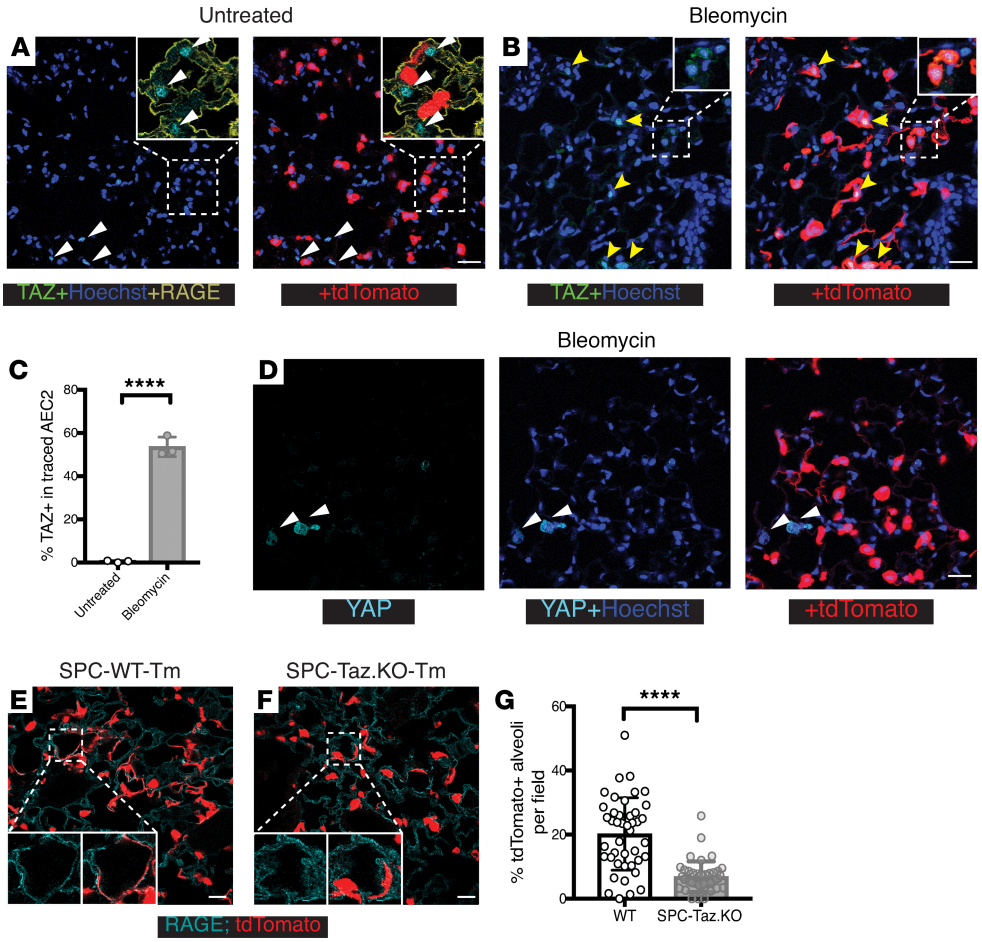

Figure 5. TAZ deficiency leads to impaired epithelial repair after bleomycin injury. (**A**–**C**) Lungs of tamoxifen-pretreated SPC-WT-Tm mice were immunostained for TAZ in untreated animals (**A**) or 10 days after bleomycin (**B**). TAZ$^+$tdTomato$^+$ traced AEC2s are indicated by yellow arrowheads in (**B**), while other TAZ$^+$ cells are indicated by white arrowheads in **A**. Insets in **A** also show RAGE costaining. Insets in **B** show cytoplasmic expression of TAZ in sporadic AEC2s. (**C**) Quantification shows the percentage (mean ± SD) of AEC2 lineage-traced cells expressing TAZ in the nuclei (n = 3 mice). Total counts: 589 AEC2s (untreated); 916 AEC2s (bleomycin). ****P < 0.0001 (unpaired 2-tailed Student's t tests). (**D**) Lungs of tamoxifen-pretreated SPC-WT-Tm mice were immunostained for YAP 10 days after bleomycin instillation. YAP is only detected in certain untraced (tdTomato$^-$) cells (white arrowheads), but not traced (tdTomato$^+$) AEC2s. (**E**–**G**) Tamoxifen pretreated SPC-WT-Tm and SPC-Taz.KO-Tm mice were immunostained 10 days after bleomycin delivery. Dashed squares delineate newly regenerated alveoli, identified by squamous AEC1s expressing AEC2 lineage tracer (tdTomato$^+$; insets). (**G**) Quantification shows the percentage (mean ± SD) of newly regenerated alveoli per image field; n = 43 randomly selected Z-stacked image fields from 3 WT mice (total 3,343 alveoli counted); n = 41 randomly selected Z-stacked image fields from 3 Taz.KO mice (total 2,482 alveoli counted). ****P < 0.0001 (unpaired 2-tailed Student's t tests). Scale bars: 30 μm.

deuterated water (D_2O) to animals from days 9 to 24 of the study to distinguish newly synthesized collagen during the course of the study (i.e., deuterated hydroxyproline) from preexisting collagen already deposited before the onset of fibrosis (20). Consistent with the increased collagen staining observed by immunofluorescence, deuterated ("new") hydroxyproline was significantly increased in lungs from SPC-Taz.KO mice compared with control mice (Figure 6B). These data suggest that TAZ deficiency in AEC2s compromises AEC2-to-AEC1 differentiation during epithelial repair, resulting in more severe fibrosis after acute bleomycin-induced lung injury.

During homeostasis, AEC1s are slowly regenerated from a rare subpopulation of AEC2s that is maintained by constitutive Wnt signaling (19). To investigate the role of TAZ in alveolar renewal during homeostasis, we examined the lungs from untreated SPC-WT-Tm and SPC-Taz.KO-Tm mice 3 months after tamoxifen induction. We did not observe significant differences in the percentages of renewal foci (Figure 6, C and D) nor in overall alveolar architecture in these uninjured lungs.

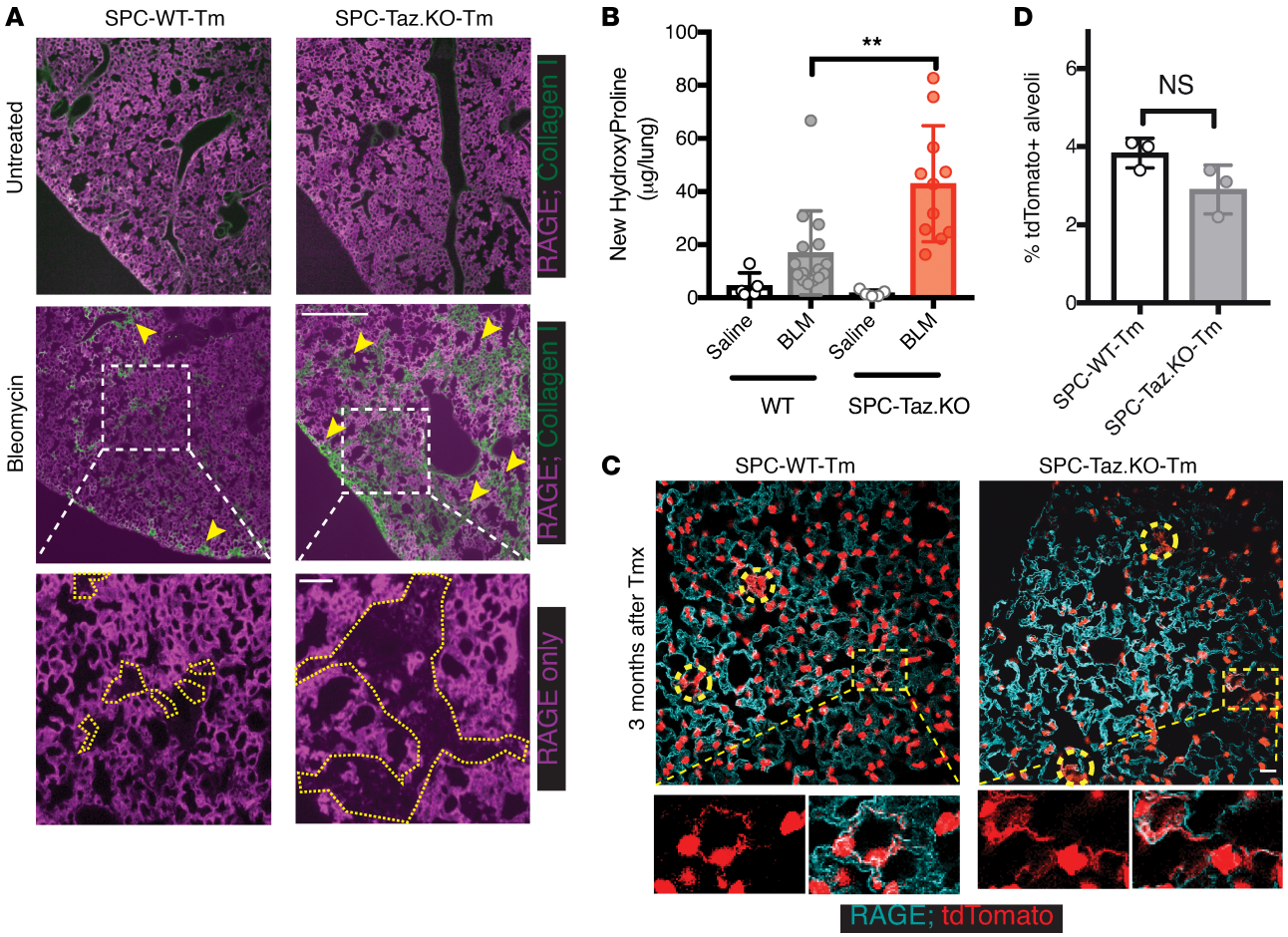

Figure 6. Fibrosis is increased in TAZ-deficient mice in response to bleomycin injury in regions with defective epithelial repair. (**A**) FL images show mouse lungs examined untreated or 22 days after bleomycin delivery. Lungs were immunostained for RAGE (AEC1) and collagen I. Arrows indicate fibrotic lesions with dense collagen deposition. Close-up images show more extensive alveolar epithelial loss (yellow polygons) in SPC-Taz.KO-Tm mouse lungs. (**B**) Deuterated hydroxyproline levels (mean ± SD) were measured as an indicator of newly synthesized collagen. $^{**}P < 0.01$ (1-way ANOVA with Tukey's test); $n = 5$ mice (each saline group); $n = 15$ mice (WT, BLM); $n = 11$ mice (SPC-Taz.KO, BLM). (**C** and **D**) SPC-WT-Tm and SPC-Taz.KO-Tm mice were examined 3 months after tamoxifen (Tmx) induction. Lungs were immunostained for RAGE and AEC2 lineage trace was indicated by tdTomato$^+$. Circles delineate newly regenerated alveoli, identified by squamous AEC1s expressing AEC2 lineage tracer (tdTomato$^+$). High-magnification insets show comparable morphologies of newly regenerated AEC1s in these two strains. (**D**) Quantification shows the percentage (mean ± SD) of newly regenerated alveoli in SPC-WT-Tm mice ($n = 3$ mice with total 3,656 alveoli counted) and SPC-Taz.KO mice ($n = 3$ mice with total 4,425 alveoli counted). NS (unpaired 2-tailed Student's t tests). Scale bars: 0.5 mm (**A**); 100 μm (**A**, enlarged); 30 μm (**C**).

Morphologically, newly regenerated AEC1s in SPC-Taz.KO-Tm mice were similar to those seen in WT mice, with a fully elongated structure (Figure 6C, close-up). These data suggest that TAZ is dispensable during normal lung homeostasis.

Soluble RAGE (sRAGE) is expressed predominantly by AEC1s and is detectable in peripheral blood. In patients with IPF, plasma sRAGE levels are decreased relative to controls (21) and may reflect AEC1 health integrated across total lung tissue. We assessed plasma sRAGE in healthy controls and a subset of IPF patients enrolled in the placebo arm of the ASCEND study (ref. 22 and Supplemental Table 1). Baseline plasma sRAGE levels were significantly lower in IPF patients than in controls (Figure 7A), and among IPF patients, they were significantly lower in those that experienced disease progression in the subsequent year than those that did not progress (Figure 7B). Plasma sRAGE levels decreased to a greater degree over 6 months in patients that progressed within a 1-year time frame compared with nonprogressors (Figure 7C). While indirect, these observations suggest that compromised AEC1 integrity, as reflected in decreased plasma sRAGE, which may be a consequence of deficient repair in response to injury, is prognostic for disease progression in IPF patients.

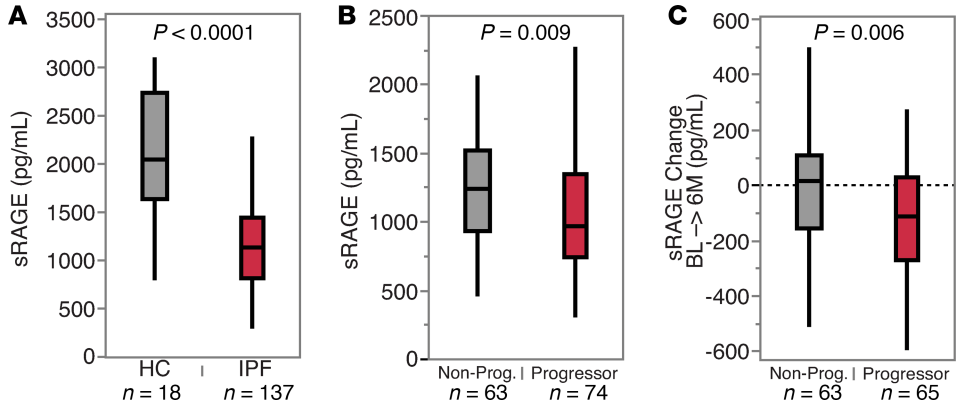

Figure 7. Decreased blood levels of RAGE were associated with more rapid disease progression in IPF patients. (**A**) Soluble RAGE levels in plasma from IPF patients and healthy controls. (**B**) Plasma sRAGE at baseline in IPF patients, dichotomized by disease progression (defined as loss of ≥10% predicted forced vital capacity [FVC] or death) from baseline to 1 year of follow-up. (**C**) Change in plasma sRAGE levels from baseline to 6 months in IPF progressors and nonprogressors. Statistical significance between the groups was determined by Wilcoxon rank sum test. BL, baseline.

Discussion

YAP and TAZ play important roles in embryonic development, homeostasis, tissue regeneration, and tumorigenesis. In particular, their activities are induced transiently upon tissue injury, which can expand progenitor cells, guide stem cell differentiation, and facilitate repair (23–27). Our study shows that TAZ is directly involved in AEC2-to-AEC1 differentiation upon alveolar epithelial injury. YAP/TAZ have been described as key transcription factors responding to mechanical stress, including cell shape and surrounding ECM stiffness. YAP/TAZ become activated (nuclear localization) when cells are at a high mechanosignaling level, e.g., growing on a rigid matrix, but remain inactive when cells are rounded and attached to a soft ECM (28). Likewise, AEC2s spontaneously differentiate to AEC1s when cultured on a stiff surface (11); while to maintain AEC2 fate, cells must be grown on a soft surface (i.e., Matrigel; ref. 29). We speculate that in vivo mechanical stress might serve as a cue for AEC2-to-AEC1 differentiation during repair. Interestingly, although YAP-deficient mice are embryonic lethal (30), TAZ-KO mice survive embryogenesis but display enlargement of the alveolar spaces across the entire lung, suggesting that TAZ may also be involved in alveolarization during development (31). Mechanical forces generated by fetal breathing are essential for AEC1 differentiation at the lung sacculation stage (32), and a recent study connected YAP/TAZ to AEC1 differentiation during lung development (33). Therefore, it is tempting to speculate that AEC1 regeneration might employ a similar mechanical stress mechanism through the YAP/TAZ pathway during both embryonic development and injury repair processes in adult lungs.

Recent studies showed that local Wnt signaling creates a stemness niche for AEC2 progenitor cells during homeostasis (19, 34). After injury, Wnt signals are induced to expand the AEC2 progenitor population, recruiting additional AEC2s to serve as progenitors. Wnt signals help AEC2s to maintain their stem cell plasticity; after proliferation and movement away from the paracrine Wnt source, AEC2s can differentiate into AEC1s (19, 34). Our data suggest that the loss of a Wnt signal is insufficient to lead to the full differentiation of AEC2s, which also requires TAZ activity in vitro and in response to injury in vivo. In a parallel context, while Wnt plays a crucial role in intestinal homeostasis, YAP is transiently upregulated upon injury and suppresses Wnt signaling. In this way, YAP inhibits the Wnt-driven homeostatic program and promotes the repair program by regulating ISC proliferation and differentiation (35–37). Although the precise molecular mechanisms whereby YAP/TAZ negatively regulate Wnt activity remain unclear, multiple models have been proposed (15, 35, 38). Cytoplasmic YAP/TAZ can limit the activity of Wnt signaling either by interacting with disheveled (DVL) or β-catenin (35, 38, 39). YAP/TAZ can also associate with the destruction complex, which is involved in the degradation of β-catenin and TAZ itself (15, 16). Intriguingly, we observed TAZ cytoplasmic expression in sporadic TAZ$^+$ AEC2s after lung injury (Figure 5B, inset). While our experimental system is insufficient to identify the precise mechanism, those cells may be in the process of differentiation by switching off the Wnt signal and turning on the TAZ signal.

YAP has been shown to be dispensable in normal gut homeostasis, while it is necessary during intestinal epithelial repair after injury (36). Likewise, our study shows that TAZ is dispensable for normal adult lung homeostasis in the absence of injury. Upon injury, normally quiescent AEC2s are recruited to act as progenitor cells to replace the lost alveolar epithelium (19). Unlike rare AEC2 stem cells during homeostasis, which depend on a fibroblast-supplied Wnt niche, these cells quickly activate autocrine Wnt activities through as-yet poorly understood mechanisms. We postulate that, along with this Wnt signal, TAZ plays an essential role for alveolar regeneration in these AEC2s by mediating the switch to AEC1 fate after proliferation. The fine tuning of these two signaling pathways helps AEC2s to proliferate and differentiate sequentially, which ultimately restores the complex tissue architecture of the alveolar epithelium.

Following the initial submission of this manuscript, a study implicating YAP and TAZ in alveolar repair after acute *Streptococcus pneumoniae* infection was published (40). Similar to our findings, that study showed that inadequate alveolar repair after acute injury contributed to increased fibrogenesis; in contrast to our findings, alveolar repair in the *S pneumoniae* model was dependent on both YAP and TAZ expression. Another recent study using a *Pseudomonas aeruginosa* acute infection model suggested a role for *Dlk-1* in downregulating Notch signaling to promote AEC2-AEC1 differentiation (41). Thus, multiple developmental pathways, including Wnt, Hippo, and Notch, work together to mediate tissue repair after alveolar injury. Previous studies examining the role of Wnt signaling in alveolar repair (19, 34, 42) used lineage-specific genetic ablation or viral infection to induce alveolar injury. Further mechanistic studies in these and other models are needed to reconcile the precise requirements for components of each pathway in space and time. In humans with IPF, evidence for increased YAP activity in cross-talk with mTOR/PI3K/AKT pathways has been suggested in alveolar epithelial cells (43). Other studies have suggested that YAP activation may contribute to increased activation of myofibroblasts (44), which, coupled with our observations and these other mechanistic studies, suggests that a proper balance, sequencing, and cell-type specificity of Wnt and Hippo pathway activity may be necessary to promote appropriate alveolar epithelial regeneration. Nevertheless, the generalizability of the observations across markedly different models suggests the fundamental nature of these pathways in tissue repair and increases the likelihood that these models are translatable to human diseases such as IPF, acute respiratory distress syndrome (ARDS), and emphysema.

Humans with IPF exhibit decreased expression of RAGE, an AEC1 marker, in lung tissue (45), and have decreased levels of sRAGE in peripheral blood compared with healthy controls (21). We confirmed that IPF patients have decreased systemic sRAGE levels compared with controls and further showed that decreasing sRAGE levels over 6 months correspond to an increased rate of lung function decline over 1 year (Figure 7). In contrast to IPF, which has chronic low-level alveolar epithelial injury and insufficient repair over a long time period, acute lung injury (ALI) and ARDS present with massive epithelial injury that can progress to death within days to weeks. Blood sRAGE levels are elevated in ARDS patients and associated with a poor prognosis (46), and a short-term spike in sRAGE after injury resolves upon ALI resolution in an animal model (47). Taken together, these observations suggest that while steady-state blood sRAGE levels may reflect overall AEC1 health, acute injury and massive AEC1 death may result in the release of significant quantities of sRAGE into the systemic circulation. On the other hand, the decreased levels of serum sRAGE in IPF are likely to reflect chronic low-level injury and inability to repair alveolar epithelium, hence the levels of this biomarker must be interpreted in specific disease contexts (48). Taken together, our observations of decreased sRAGE in IPF associated with disease progression are consistent with IPF representing a condition of a chronically inadequate capacity to regenerate alveolar epithelium, which predisposes to an excessive interstitial fibrotic response.

We observed exacerbated fibrosis resulting from inadequate repair of lung alveolar epithelial injury. This provides a key mechanistic link between the loss of alveolar epithelial regenerative capacity and fibrogenesis. Our study adds to an emerging body of work characterizing the importance of developmental pathways, including Wnt, Notch, and Hippo, in adult lung epithelial repair and regeneration after injury. Future studies elucidating the cross-talk between these mechanisms may have therapeutic implications for interstitial lung disorders, such as IPF, ARDS, and emphysema, by enabling interventions that promote proper alveolar epithelial regeneration to reestablish intact tissue architecture.

Methods

Animals. SPC-CreERT2; Rosa-lsl-tdTomato (SPC-WT-Tm) mice were provided by Brigid Hogan (Duke University, Durham, North Carolina) (8). This strain was bred to *Taz*$^{fl/fl}$ mice (made at Genentech) to generate SPC-CreERT2; *Taz*$^{fl/fl}$; Rosa-lsl-tdTomato (SPC-Taz.KO-Tm) mice. Induction of CreERT2 alleles was done by i.p. injecting 80 mg/kg tamoxifen (T5648; MilliporeSigma) in sunflower seed oil (S5007-1L; MilliporeSigma) for 5 consecutive days. Subsequent studies were initiated at least 1 week after the completion of tamoxifen treatment. *Ctnnb1*$^{fl/fl}$ (catalog 004152) and C57BL/6 (C57B6, as WT) mice were both from The Jackson Laboratory.

Lung cell isolation and AEC2 sorting. Lung cells were isolated following a previously published protocol with minor modifications (49). Tissues were disrupted and single cells were collected after lungs were inflated and digested with a protease solution cocktail (5 U/mL dispase, 450 U/mL collagenase type I, 4 U/mL elastase, and 0.33 U/mL DNase I in DMEM/F12; ref. 49) for 45 minutes at 37°C with frequent agitation. Cells were then washed by DMEM with 10% FBS (Invitrogen) and resuspended in ACK lysis buffer for 3 minutes to lyse red blood cells. For samples without the lineage-tracing marker (from *Ctnnb1*$^{fl/fl}$, Cre$^-$ Rosa-lsl-tdTomato, or C57B6 mice), cells were first resuspended in DMEM plus 10% FBS containing LysoTracker Green DND-26 (50 nM, L7526; Invitrogen) at 37°C for 45 minutes (17). After washing, cells were blocked by purified rat anti-mouse CD16/CD32 antibody (553142; BD Biosciences) and stained with antibodies for CD45 (17-0451-82, eBioscience), EpCAM (11-5791-82, eBioscience). AEC2s were sorted on a BD FACSAria Fusion cell sorter (BD Biosciences), based on the following markers: CD45$^-$, EpCAM$^+$, Lysotracker$^+$, or tdTomato$^+$. Data were analyzed by Flowjo software.

AEC 3D organoid culture. AEC organoid culture was performed by following a previously published protocol with minor modifications (8). Sorted AEC2s were mixed with NHLFs (CC-2512; Lonza Walkersville Inc.) at a 1:10 ratio. The cells were resuspended in a prechilled 1:1 mixture of mouse tracheal epithelial cells (MTEC)/Plus medium (50) and growth factor–reduced Matrigel (356231; BD Biosciences). 10^4 AEC2s and 10^5 NHLF cells were placed in 90 μL mixed media in a 24-well 0.4-μm Transwell insert (3470; Costar). 500 μL MTEC/Plus media was added to the lower chamber, with the following compounds added at 10 μM at the beginning of the culture when indicated: IWR-1 (3532, R&D Systems); PJ-34 (P4365), PNU-74654 (P0052); IWR-1-exo (3947, R&D Systems); XAV939 (X3004); and JW55 (SML0630). All compounds other than IWR-1 and IWR-1-exo were from MilliporeSigma. Media were changed every other day. We determined that a ROCK inhibitor (Y-27632) was not required in this culture, and therefore it was not added.

Adenovirus Cre–mediated gene deletion in the organoid culture. Adenovirus expressing Cre recombinase (Ad-CMV-iCre, 1045, Vector Biolabs) or control (catalog 1240) was diluted and mixed with AEC2s and NHLF cells at MOI = 3 (e.g., 3×10^5 PFU per insert) and plated into Transwell inserts at the beginning of the culture. No virus was added in the lower chamber.

Cell isolation and staining from organoid culture. Spheroids were dissociated from Matrigel after treatment with 1 mL dispase solution (5 U/mL, 354235; Corning) in DMEM/F12 (1:1) media at 37°C for 30 minutes. After washing with PBS, cells were incubated in 0.05% Trypsin-EDTA (25300, Gibco) for 10 minutes at 37°C to create a single-cell suspension. Cells were then washed and stained for EpCAM. For intracellular staining, the BD Cytofix/Cytoperm Fixation/Permeabilization Solution kit was used (554714; BD Biosciences). Following the manufacturer's recommendations, cells were stained intracellularly with an antibody for β-catenin (50-2567-42; eBiosciences) after fixation and permeabilization. FACS was performed on a BD LSR II flow cytometer (BD Biosciences), and data were analyzed by FlowJo software.

EdU labeling and flow cytometry. AEC organoid cultures were treated with either control or IWR-1 as before. At day 6, cultures were pulsed with 10 μM EdU for 2 hours. Cells were collected and stained following manufacturer's recommendations (c10419, Molecular Probes). The percentages of EdU$^+$ cells were calculated based on the total tdTomato$^+$ cells harvested.

RNA isolation and quantitative RT-PCR from organoid culture. RNA was isolated from the organoid culture immediately after spheroids were dissociated from Matrigel by dispase (see above), using the RNeasy Mini Kit (74106; Qiagen). Gene expression levels were quantified by RT-qPCR using Taqman RNA-to-C_T 1-Step Kit (4392938; Applied Biosystems). The reactions were run on a QuantStudio 6 Flex Real-Time PCR System (Thermo Fisher). Threshold cycle values (Ct) were normalized to a housekeeping gene, GAPDH (ΔCT). The relative gene expression levels of the 2 cell types (AEC2 vs. AEC1) were calculated by the $2^{-\Delta\Delta CT}$ method. The following Taqman gene expression assay kits from Applied Biosystems were used: *Hopx* (Mm00558630_m1), *Spc* (Mm00488144_m1), *Pdpn* (Mm01348912_g1), Aqp5 (Mm00437579_m1), *Taz* (Mm01289581_g1), and *Gapdh* mouse (4352661).

Whole-spheroid culture and immunostaining. To perform the whole-spheroid immunostaining, the organoid culture conditions were modified. Three thousand AEC2s and 30,000 NHLF cells were seeded in 30 μL 100% Matrigel per Transwell insert and cultured as described above. After culturing, inserts were removed and washed with PBS and fixed with 4% paraformaldehyde for 2 hours at room temperature. The bottoms of the inserts were removed with a blade, and the solidified Matrigel was released from the Transwell inserts. The solidified gel was washed with PBS and blocked and permeabilized with PBS plus 0.5% Triton X-100 plus 5% donkey serum (PTS) for 2 hours at room temperature. Primary and secondary antibodies were used sequentially to immunostain the gel at 4°C for overnight each time. The gel was washed 3 times with PBS plus 0.5%Triton X-100 (2 hours each wash) at room temperature after each staining step. To mount the Matrigel, adhesive tape was used to raise the edge of the glass slide to create a space between the slide and the cover glass. The gel was then placed in the middle of the slide and Fluoromount-G (0100-01; SouthernBiotech) was used as the mounting media.

AEC2 culture on tissue culture treated plates. Sorted AEC2s (>95% purity) were directly cultured in 8-well cell culture–treated chamber slides (154534, Labtek) in DMEM media with 10% FBS. 10^5 cells in 300 μL media were used per well, in the presence of 10 μM IWR-1 when indicated. Media were changed every other day. The cells were cultured for 5 days before imaging analysis.

Genomic DNA isolation from sorted AEC2s and quantitative PCR. Genomic DNA was isolated from sorted AEC2s using the DNeasy Blood & Tissue Kit (69506; Qiagen). *Taz* DNA levels were quantified by qPCR using Taqman Copy Number Assays (Applied Biosystems). Threshold cycle values (Ct) were normalized to an internal reference, *Tert* (ΔCT). The genomic DNA levels were calculated by the $2^{-\Delta\Delta CT}$ method. The following Taqman assays from Applied Biosystems were used: *Taz* (Mm00551695_cn) and *Tert* (4458373).

Lung sections. After mice were euthanized, lungs and trachea were removed. Lung lobes were inflated and fixed with 4% paraformaldehyde overnight at 4°C. Afterward, lungs were submerged in 15% and 30% sucrose at 4°C overnight sequentially for cryoprotection, before embedding in Tissue Freezing Medium (TFM-5; General Data Company). Frozen tissues were cryosectioned (12 μm) using a Cryostat (Leica CM3050S).

Lineage-tracing and cell analysis. To examine TAZ^+ and $Ki67^+$ $tdTomato^+$ AEC2s, 12-μm *Z*-stacked images were captured in random fields with a ×40 objective (Leica PL APO CS ×40) and a ×20 objective (Leica PL APO CS ×20), respectively. The percentages of positively stained cells were calculated and averaged. Lung alveoli were quantified by scoring forty 12-μm *Z*-stacked random fields. Newly regenerated alveoli were determined by the presence of AEC2-traced ($tdTomato^+$) AEC1s in the alveoli. The percentage of new alveoli in each image was calculated and plotted.

Microscopy. Images with a *Z*-stack of multiple optical sections were captured on a Leica TCS SPE spectral confocal microscope. Images were processed and analyzed by ImageJ (NIH). Cells in the all *Z*-planes were counted by the manual cell counter function in ImageJ. The organoid whole plate culture images and lung lobe images were captured on a Nikon Ti-E Perfect Focus inverted microscope. Large images were generated by automatically stitching multiple adjacent frames from a multipoint acquisition using a motorized stage. Images were analyzed by ImageJ software (NIH).

Imaging antibodies. The following primary antibodies were used in immunostaining against various antigens: pro-SPC (sc-7706; Santa Cruz Biotechnology), HOPX (sc-30216; Santa Cruz Biotechnology), PDPN (14-5381-85; eBioscience), AQP5 (178615; Calbiochem), Ki67 (ab16667; Abcam), RAGE (MAB1179; R&D Systems), Collagen I (ab34710; Abcam), YAP1 (14074S; Cell Signaling), TAZ (HPA007415; MilliporeSigma). Primary antibodies (1:100) were detected by Alexa Fluor–labeled Donkey secondary antibodies (1:500; Invitrogen) with Hoechst 33342 (1:1000, H3570; Invitrogen, 1:1000).

Bleomycin administration, deuterated water labeling, and hydroxyproline measurement. Adult mice (older than 12 weeks) were randomized based on their weights before the study to minimize variance between experimental and control groups. For i.t. dosing, all mice were lightly anesthetized with isoflurane in an induction chamber. Once anesthetized, the animals were removed from the chamber, manually restrained, the mouth of the animal was opened and the tongue set aside. A 1-mL syringe with 50 μL sterile injectable isotonic saline or bleomycin (0.70 U/kg, DNC 0703-3155-01; TEVA) in 50 μL sterile isotonic saline) was connected to a 24-gauge gavage needle. The gavage needle was inserted into the trachea and a dose of either vehicle or bleomycin was delivered i.t. After delivery, animals were monitored continuously until fully awake and ambulatory.

Deuterated water labeling was used previously to assess the new collagen synthesis in bleomycin studies (20). In our studies, the labeling was started at day 9 after bleomycin delivery (51), by i.p. injecting deuterated

water (DLM-4-99.8-1000; Cambridge Isotope Laboratories) 35 mL/kg in 2 divided doses 4 hours apart. Afterward, 8% deuterated water in drinking water was provided ad lib in a water bottle until the end of the study.

Deuterated water incorporation into hydroxyproline was analyzed as described previously (52). Mass spectrometry and analysis were performed by Metabolic Solutions. New hydroxyproline content was expressed as μg per lung.

Analysis of human samples. For human plasma samples, IPF patients described in this study are a subset of the ASCEND study and are reported in detail previously (53). For measuring circulating sRAGE levels, residual EDTA anticoagulated plasma available from a subset of the placebo arm of the ASCEND cohort was used. Specifically, to pick progressors, we included all patients from the placebo arm, where residual sample was available AND the patient showed substantial disease progression, as defined by either death or reduction in percent-predicted forced vital capacity by 10 units or more between baseline to 12 months of follow-up. To pick an equivalent number of nonprogressors, we sampled randomly from the remaining patients in the placebo arm that did not meet the progressor definition. Age- and sex-matched nondiseased control samples were procured commercially (BioIVT). For plasma sRAGE measurement, sRAGE was measured from plasma using a Luminex kit from R&D Systems, with methods optimized from manufacturer's recommendations.

Statistics. Data are expressed as the mean ± SEM. All experiments were repeated 2 or more times. No animals were excluded from analysis in any experiment. Data and statistical analyses were done with Prism 7 (GraphPad Software). Variable differences between experimental and control groups were assessed using the 2-tailed Student's *t* tests. One-way ANOVA followed by Tukey's test was used for multiple-comparisons. A P value less than 0.05 was considered significant. Biological replicates were conducted using different animals that were sex- and age-matched when comparing among different groups.

Study approval. All animal experiments were approved by the Institutional Animal Care and Use Committee at Genentech Inc. The ASCEND study was approved by independent ethics committees and institutional review boards (see Supplemental Appendix A of ref. 53 for the names of the institutions that provided approval) and by InterMune Inc. or designees. Written informed consent was given for biomarker analysis.

Author contributions

JGE conceived and guided the initial screen. TS led the subsequent studies. TS designed, performed, and analyzed experiments, and drafted the manuscript. ZH and HZ performed and MX and HB supervised in vivo mouse experiments. HB analyzed the in vivo hydroxyproline data. CP assisted with confocal microscopy experiments. GJ and TRR performed experiments with and analyzed human biomarker data. AD designed and generated *Taz*$^{fl/fl}$ mice and gave experimental advice. JRA supervised the study, provided scientific insight, and reviewed and edited the manuscript.

Acknowledgments

We thank Brigid Hogan for providing SPC-WT-Tm mice; Nobuhiko Kayagaki for providing β-catenin$^{fl/fl}$ mice; Steve Kauder, Elsa Ndiaye-Dulac, and Ying Xi for helpful discussions; and Genentech core laboratories for technical assistance. This work was supported by Genentech.

Address correspondence to: Tianhe Sun or Joseph Arron, 1 DNA Way, South San Francisco, California 94080, USA. Phone: 650.225.6432; Email: sun.tianhe@gene.com (TS). Phone: 650.467.8871; Email: arron.joseph@gene.com (JA).

CP's present address is: Department of Bioengineering, UCSD, La Jolla, California, USA.

JGE's present address is: Department of Oncology, Amgen Inc., South San Francisco, California, USA.

1. Garcia CK. Insights from human genetic studies of lung and organ fibrosis. *J Clin Invest*. 2018;128(1):36–44.
2. Kim CF, et al. Identification of bronchioalveolar stem cells in normal lung and lung cancer. *Cell*. 2005;121(6):823–835.
3. McQualter JL, Yuen K, Williams B, Bertoncello I. Evidence of an epithelial stem/progenitor cell hierarchy in the adult mouse lung. *Proc Natl Acad Sci U S A*. 2010;107(4):1414–1419.
4. Zuo W, et al. p63(+)Krt5(+) distal airway stem cells are essential for lung regeneration. *Nature*. 2015;517(7536):616–620.
5. Vaughan AE, et al. Lineage-negative progenitors mobilize to regenerate lung epithelium after major injury. *Nature*.

2015;517(7536):621–625.
6. Evans MJ, Cabral LJ, Stephens RJ, Freeman G. Transformation of alveolar type 2 cells to type 1 cells following exposure to NO2. *Exp Mol Pathol*. 1975;22(1):142–150.
7. Evans MJ, Cabral LJ, Stephens RJ, Freeman G. Renewal of alveolar epithelium in the rat following exposure to NO2. *Am J Pathol*. 1973;70(2):175–198.
8. Barkauskas CE, et al. Type 2 alveolar cells are stem cells in adult lung. *J Clin Invest*. 2013;123(7):3025–3036.
9. Desai TJ, Brownfield DG, Krasnow MA. Alveolar progenitor and stem cells in lung development, renewal and cancer. *Nature*. 2014;507(7491):190–194.
10. Huang SM, et al. Tankyrase inhibition stabilizes axin and antagonizes Wnt signalling. *Nature*. 2009;461(7264):614–620.
11. Dobbs LG. Isolation and culture of alveolar type II cells. *Am J Physiol*. 1990;258(4 Pt 1):L134–L147.
12. Paine R, Simon RH. Expanding the frontiers of lung biology through the creative use of alveolar epithelial cells in culture. *Am J Physiol*. 1996;270(4 pt 1):L484–L486.
13. Borok Z, et al. Keratinocyte growth factor modulates alveolar epithelial cell phenotype in vitro: expression of aquaporin 5. *Am J Respir Cell Mol Biol*. 1998;18(4):554–561.
14. Thorsell AG, et al. Structural basis for potency and promiscuity in poly(ADP-ribose) polymerase (PARP) and tankyrase inhibitors. *J Med Chem*. 2017;60(4):1262–1271.
15. Azzolin L, et al. Role of TAZ as mediator of Wnt signaling. *Cell*. 2012;151(7):1443–1456.
16. Azzolin L, et al. YAP/TAZ incorporation in the β-catenin destruction complex orchestrates the Wnt response. *Cell*. 2014;158(1):157–170.
17. Van der Velden JL, Bertoncello I, McQualter JL. LysoTracker is a marker of differentiated alveolar type II cells. *Respir Res*. 2013;14:123.
18. Alcorn JL, Smith ME, Smith JF, Margraf LR, Mendelson CR. Primary cell culture of human type II pneumonocytes: maintenance of a differentiated phenotype and transfection with recombinant adenoviruses. *Am J Respir Cell Mol Biol*. 1997;17(6):672–682.
19. Nabhan AN, Brownfield DG, Harbury PB, Krasnow MA, Desai TJ. Single-cell Wnt signaling niches maintain stemness of alveolar type 2 cells. *Science*. 2018;359(6380):1118–1123.
20. Blaauboer ME, et al. Novel combination of collagen dynamics analysis and transcriptional profiling reveals fibrosis-relevant genes and pathways. *Matrix Biol*. 2013;32(7-8):424–431.
21. Manichaikul A, et al. Plasma soluble receptor for advanced glycation end products in idiopathic pulmonary fibrosis. *Ann Am Thorac Soc*. 2017;14(5):628–635.
22. Neighbors M, et al. Prognostic and predictive biomarkers for patients with idiopathic pulmonary fibrosis treated with pirfenidone: post-hoc assessment of the CAPACITY and ASCEND trials. *Lancet Respir Med*. 2018;6(8):615–626.
23. Wang Y, Yu A, Yu FX. The Hippo pathway in tissue homeostasis and regeneration. *Protein Cell*. 2017;8(5):349–359.
24. Dupont S, et al. Role of YAP/TAZ in mechanotransduction. *Nature*. 2011;474(7350):179–183.
25. Cai J, Zhang N, Zheng Y, de Wilde RF, Maitra A, Pan D. The Hippo signaling pathway restricts the oncogenic potential of an intestinal regeneration program. *Genes Dev*. 2010;24(21):2383–2388.
26. Grijalva JL, et al. Dynamic alterations in Hippo signaling pathway and YAP activation during liver regeneration. *Am J Physiol Gastrointest Liver Physiol*. 2014;307(2):G196–G204.
27. Leach JP, et al. Hippo pathway deficiency reverses systolic heart failure after infarction. *Nature*. 2017;550(7675):260–264.
28. Panciera T, Azzolin L, Cordenonsi M, Piccolo S. Mechanobiology of YAP and TAZ in physiology and disease. *Nat Rev Mol Cell Biol*. 2017;18(12):758–770.
29. Gonzalez RF, Dobbs LG. Isolation and culture of alveolar epithelial Type I and Type II cells from rat lungs. *Methods Mol Biol*. 2013;945:145–159.
30. Morin-Kensicki EM, et al. Defects in yolk sac vasculogenesis, chorioallantoic fusion, and embryonic axis elongation in mice with targeted disruption of Yap65. *Mol Cell Biol*. 2006;26(1):77–87.
31. Mitani A, Nagase T, Fukuchi K, Aburatani H, Makita R, Kurihara H. Transcriptional coactivator with PDZ-binding motif is essential for normal alveolarization in mice. *Am J Respir Crit Care Med*. 2009;180(4):326–338.
32. Li J, Wang Z, Chu Q, Jiang K, Li J, Tang N. The strength of mechanical forces determines the differentiation of alveolar epithelial cells. *Dev Cell*. 2018;44(3):297–312.e5.
33. Zhou B, et al. Claudin-18-mediated YAP activity regulates lung stem and progenitor cell homeostasis and tumorigenesis. *J Clin Invest*. 2018;128(3):970–984.
34. Zacharias WJ, et al. Regeneration of the lung alveolus by an evolutionarily conserved epithelial progenitor. *Nature*. 2018;555(7695):251–255.
35. Barry ER, et al. Restriction of intestinal stem cell expansion and the regenerative response by YAP. *Nature*. 2013;493(7430):106–110.
36. Gregorieff A, Liu Y, Inanlou MR, Khomchuk Y, Wrana JL. Yap-dependent reprogramming of Lgr5(+) stem cells drives intestinal regeneration and cancer. *Nature*. 2015;526(7575):715–718.
37. Imajo M, Ebisuya M, Nishida E. Dual role of YAP and TAZ in renewal of the intestinal epithelium. *Nat Cell Biol*. 2015;17(1):7–19.
38. Imajo M, Miyatake K, Iimura A, Miyamoto A, Nishida E. A molecular mechanism that links Hippo signalling to the inhibition of Wnt/β-catenin signalling. *EMBO J*. 2012;31(5):1109–1122.
39. Varelas X, et al. The Hippo pathway regulates Wnt/β-catenin signaling. *Dev Cell*. 2010;18(4):579–591.
40. LaCanna R, et al. Yap/Taz regulate alveolar regeneration and resolution of lung inflammation. *J Clin Invest*. 2019;130:2107–2122.
41. Finn J, et al. Dlk1-mediated temporal regulation of Notch signaling is required for differentiation of alveolar type II to type I cells during repair. *Cell Rep*. 2019;26(11):2942–2954.e5.
42. Lee JH, et al. Anatomically and functionally distinct lung mesenchymal populations marked by Lgr5 and Lgr6. *Cell*. 2017;170(6):1149–1163.e12.
43. Gokey JJ, et al. Active epithelial Hippo signaling in idiopathic pulmonary fibrosis. *JCI Insight*. 2018;3(6):98738.
44. Liu F, et al. Mechanosignaling through YAP and TAZ drives fibroblast activation and fibrosis. *Am J Physiol Lung Cell Mol Physiol*. 2015;308(4):L344–L357.
45. Queisser MA, et al. Loss of RAGE in pulmonary fibrosis: molecular relations to functional changes in pulmonary cell types.

Am J Respir Cell Mol Biol. 2008;39(3):337–345.
46. Uchida T, et al. Receptor for advanced glycation end-products is a marker of type I cell injury in acute lung injury. *Am J Respir Crit Care Med*. 2006;173(9):1008–1015.
47. Patel BV, Wilson MR, Takata M. Resolution of acute lung injury and inflammation: a translational mouse model. *Eur Respir J*. 2012;39(5):1162–1170.
48. Oczypok EA, Perkins TN, Oury TD. All the "RAGE" in lung disease: The receptor for advanced glycation endproducts (RAGE) is a major mediator of pulmonary inflammatory responses. *Paediatr Respir Rev*. 2017;23:40–49.
49. Rock JR, et al. Multiple stromal populations contribute to pulmonary fibrosis without evidence for epithelial to mesenchymal transition. *Proc Natl Acad Sci U S A*. 2011;108(52):E1475–E1483.
50. Rock JR, et al. Basal cells as stem cells of the mouse trachea and human airway epithelium. *Proc Natl Acad Sci U S A*. 2009;106(31):12771–12775.
51. Moeller A, Ask K, Warburton D, Gauldie J, Kolb M. The bleomycin animal model: a useful tool to investigate treatment options for idiopathic pulmonary fibrosis? *Int J Biochem Cell Biol*. 2008;40(3):362–382.
52. Gardner JL, Turner SM, Bautista A, Lindwall G, Awada M, Hellerstein MK. Measurement of liver collagen synthesis by heavy water labeling: effects of profibrotic toxicants and antifibrotic interventions. *Am J Physiol Gastrointest Liver Physiol*. 2007;292(6):G1695–G1705.
53. King TE, et al. A phase 3 trial of pirfenidone in patients with idiopathic pulmonary fibrosis. *N Engl J Med*. 2014;370(22):2083–2092.